A merged continental planetary boundary layer height dataset based on high-resolution radiosonde measurements, ERA5 reanalysis, and GLDAS

Jianping Guo[a]★, Jian Zhang[b*], Jia Shao[d]★, Tianmeng Chen[a], Kaixu Bai[c], Jia Shao[d*], Yuping Sun[a], Ning Li[a], Jingyan Wu[a], Rui Li[e], Jian Li[a], Qiyun Guo[f], Jason B. Cohen[g], Panmao Zhai[a], Xiaofeng Xu[h], Fei Hu[i*]

[a]State Key Laboratory of Severe Weather, Chinese Academy of Meteorological Sciences, Beijing 100081, China
[b]Hubei Subsurface Multi-scale Imaging Key Laboratory, Institute of Geophysics and Geomatics, China University of Geosciences, Wuhan 430074, China
[c]Key Laboratory of Geographic Information Science (Ministry of Education), School of Geographic Sciences, East China Normal University, Shanghai 200241, China
[d]College of Informatics, Huazhong Agricultural University, Wuhan 430070, China
[e]Ministry of Education Key Laboratory for Earth System Modeling, Department of Earth System Science, Tsinghua University, Beijing 100084, China
[f]Meteorological Observation Center, China Meteorological Administration, Beijing 100081, China
[g]School of Environment and Spatial Informatics, China University of Mining and Technology, Xuzhou, China
[h]China Meteorological Administration, Beijing 100081, China
[i]State Key Laboratory of Atmospheric Boundary Layer Physics and Atmospheric Chemistry, Institute of Atmospheric Physics, Beijing 100029, China

★Both authors Jianping Guo and Jia Shao contributed equally and should be considered co-first authors.

Correspondence to:
Dr. Jian Zhang (Email: zhangjian@cug.edu.cn), Dr. Jia Shao (Email: shaojia@mail.hzau.edu.cn and Dr./Prof. Fei Hu (Email: hufei@mail.iap.ac.cn)

带格式的: 两端对齐

设置了格式: 字体: (中文) Times New Roman

ABSTRACT

The planetary boundary layer (PBL) is the lowermost part of the troposphere that governs the exchange of momentum, mass and heat between surface and atmosphere. To date the radiosonde measurements have been extensively used to estimate PBLH; suffering from low spatial coverage and temporal resolution, the radiosonde data is incapable of providing the diurnal description of PBLH across the globe. To fill this data gap, this paper aims to produce a temporally continuous PBLH dataset during the course of a day over the global land by applying the machine learning algorithms to integrate high-resolution radiosonde measurements, ERA5 reanalysis, and the Global Land Data Assimilation System (GLDAS) ~~(NASA Global Land Data Assimilation System~~ product. This dataset covers the period from 2011 to 2021 with a temporal resolution of 3-hour and a horizontal resolution of 0.25°×0.25°. The radiosonde dataset contained around 180 million profiles over 370 stations across the globe. The machine learning model was established by taking 18 parameters derived from ERA5 reanalysis and GLDAS as input variables while the PBLH biases between radiosonde observations and ERA5 reanalysis were used as the learning targets. The input variables were presumably representative regarding the land properties, near-surface meteorological conditions, terrain elevations, lower tropospheric stabilities, and solar cycles. Once a state-of-the-art model had been trained, the model was then used to predict the PBLH bias at other grids across the globe with parameters acquired or derived from ERA5 and GLDAS. Eventually, the merged PBLH can be taken as the sum of the predicted PBLH bias and the PBLH retrieved from ERA5 reanalysis. Overall, this merged high-resolution PBLH dataset was globally consistent with the PBLH retrieved from radiosonde observations both in magnitude and spatiotemporal variation, with a mean bias of as low as –0.9 m. The dataset and related codes are publicly available at https://doi.org/10.5281/zenodo.6498004 (Guo et al., 2022), which are of significance for a multitude of scientific research and applications, including air quality, convection initiation, climate and climate change, just to name a few.

设置了格式: 字体: (中文) +中文正文 (等线)

1. Introduction

Planetary boundary layer (PBL), the lowermost part of the troposphere where the turbulence and convection mainly occur, is of significance in modulating the exchange of momentum, heat, moisture, and mass between the surface and the free atmosphere over a range of scales (Stull 1988; Cooper and Eichinger, 1994; Edson et al., 2013). The turbulence in the PBL is largely generated mechanically, which is owing to both wind shear and friction, and is generated convectively, which is owing to buoyancy and surface heating (Degrazia et al., 2020). Within the PBL, vertical turbulent mixing of air masses is rapid and constant, on the order of 30 minutes or less (Wallace and Hobbs, 2006). Therefore, the reliable parameterization of the PBL is crucial for the accurate representations of vertical diffusion, cloud formation/development, and pollutant deposition in numerical weather prediction (NWP), climate, air quality and coupled atmosphere–hydrosphere–biosphere models (Seibert, 2000; Hu et al., 2010; Baklanov et al., 2011). It has been well recognized that the variation of PBL height (PBLH) significantly impacts the near-surface air quality (Petäjä et al., 2016; Wang and Wang, 2016; Lou et al., 2019; Li et al., 2021) and climate system as well (Esau and Zilitinkevich, 2010; Davy and Esau, 2016).

The development of PBL is subject to the changes of the energy balance near the ground surface, largely through the linkages between soil moisture and sensible heat flux, latent heat flux and net radiation (Dirmeyer et al., 2014; Xu et al., 2021). In particular, the sensible heat flux is closely associated with the variation in evapotranspiration, land type, and cloud cover. Also, the daytime convective PBL is modulated by cloud radiative effects, particularly in the early afternoon (Guo et al., 2016; Zhang et al., 2018; Davis et al., 2020). Furthermore, the aerosol radiative effect (due to both aerosol scattering and absorption) indirectly affects the evolution of PBL by changing the atmospheric heating rate and the solar radiation reaching the surface

(Wang et al., 2013; Li et al., 2017; Yang et al., 2016). Besides, the entrainment of air from above the PBL can also significantly drive the evolution of PBL (Hu et al., 2010).

To date, a variety of methods have been applied on vertical profiles of aerosol properties, water vapor, temperature, refractivity, and wind to estimate PBLH (e.g., Holzworth 1964; Seibert 2000; Lammert and Bösenberg 2006; McGrath-Spangler and Denning 2012; Chan and Wood 2013; Su et al., 2018; Liu et al., 2019; Ding et al., 2021). The estimate varies considerably with data sources, algorithms, and data vertical resolutions (Seibert et al., 2000; Seidel et al., 2010). For instance, PBLH determined by the minimum vertical gradient relative humidity is about 1 km larger than that from the parcel method, even though the latter algorithm is generally thought to be one of the most reliable methods for the estimation of the convective boundary layer (CBL) height (Hennemuth and Lammert, 2006; Seidel et al., 2010). In addition, different data sources, such as ceilometer Lidar, COSMIC GPS RO satellite, radiosonde, and the fifth generation ECMWF (European Centre for Medium-Range Weather Forecasts) atmospheric reanalysis (ERA5) ERA5 reanalysis dataset can reach quite different estimates of PBLH (Saha et al., 2022). Recently, as suggested by Teixeira et al. (2021), the PBLH should be ideally estimated using direct observations of vertical profiles of turbulent quantities, which is due in large part to the turbulent nature of PBL. But only a few places have such observations. A wide range of complex physical and chemical processes involved in the PBL further make PBLH estimates quite elusive and tricky (Seidel et al., 2010; Teixeira et al., 2021).

Among the instruments, radiosonde is the most accepted instrument for deriving the PBLH for both CBL and stable boundary layer (SBL), due to theits unprecedented capability of providing in situ observations of ability to characterize the thermodynamic and dynamic states of the boundary layerPBL (Seidel et al., 2010; de Arruda Moreira et al., 2018, Guo et al., 2019). In addition, the bulk Richardson number method has been proved to be the most suitable PBLH algorithm for application to a large radiosonde dataset (Seidel et al., 2012). The dataset with a full vertical resolution (5–8 m) has previously been used to study PBLHs over China and near-globe (Guo et al., 2016; 2021). The limitation of this dataset is its poor coverage over the ocean and some continental areas without high-resolution~~t~~ radiosonde observations~~, such as Africa and Central Asia~~.

By contrast, reanalysis datasets, such as ~~the fifth generation ECMWF (European Centre for Medium-Range Weather Forecasts) atmospheric reanalysis (~~ERA5~~)~~ reanalysis and the Modern-Era Retrospective-analysis for Research and Applications version 2 product (MERRA-2), have a unique advantage in spatial-temporal coverage. Our recent study (Guo et al., 2021) suggests that ERA5 is the most promising reanalysis data source in terms of characterizing the evolution of PBLH, with an underestimation of daytime PBLH at around 130 m, when compared to high-resolution radiosonde ~~(Guo et al., 2021)~~. Nevertheless, the underestimation of PBLH in ERA5 reanalysis can be as high as 500 m in the afternoon when the PBL is fully developed. This underestimation could be attributed to, but not limited to, the gradient of terrain elevation and the lower tropospheric stability. P~~—~~articularly, a~~A~~ higher terrain gradient or a more unstable troposphere generally lead to a lower PBLH in ERA5 reanalysis.

Rather, by exploiting both the advantages of in situ atmospheric measurements from radiosonde and the high-resolution model products from ERA~~-~~5 reanalysis, it is quite desirable to generate a new PBLH dataset by seamlessly blending these versatile products. The biases between PBLHs retrieved from the ERA~~-~~5 and radiosonde could be represented by the land properties, near-surface meteorological conditions, ~~etc~~among others, and further be minimized or optimized via a machine learning model. ~~optimized via a machine learning model.~~ The Global Land Data Assimilation System (GLDAS) incorporates satellite- and ground-based observations and produces a global, high-resolution product regarding land states and fluxes (Rodell et al., 2004). To this end, the present analyses used the radiosonde dataset that contained around 180 million profiles over 370 stations across the world, ~~as well as~~in combination with the ERA5 reanalysis~~,~~ and GLDAS data. A long-term merged PBLH dataset covering the period 2011 to 2021 were generated, which could have crucial implications for the development and evaluation of weather and climate, environmental meteorology, and boundary layer parameterization. The rest of the paper is organized as follows. Section 2 describes the fundamental data sets and the PBLH methodology we use in this study, Sections 3 and 4 report on the machine learning algorithm used to generate the merged PBLH dataset, also revealed are the data quality, and Section 5 represents the climatological merged continental PBLH, and Section 6 ends with a brief summary and conclusion.

2. Data sources and conventional PBLH determination method

2.1 High-resolution radiosonde measurements

As described in Guo et al. (2021) and Zhang et al. (2022), a high-resolution radiosonde dataset gained from several organizations was adopted, spanning the years from 2011 to 2021. The organizations include the China Meteorological Administration (CMA), the National Oceanic and Atmospheric Administration (NOAA), the Global Climate Observing System (GCOS) Reference Upper-Air Network (GRUAN), the Centre for Environmental Data Analysis of the United Kingdom (CEDA), University of Wyoming, and German Deutscher Wetterdienst. The detailed information on the provided data is listed in Table 1. In total,- over 185 million -radiosonde profiles were collected to determine PBLH, 95% of which were released at regular synoptic times of 0000 UTC and 1200 UTC, and the rest of them which were irregularly launched at other times during the intensive observational periods. Note that those soundings with the lowest burst height lower than 10 km above ground level (a.g.l) were eliminated. In addition, all the original profiles soundings were evenly interpolareted to the profiles with a 10 m vertical resolution of 10 min altitudethe vertical direction by cubic spline interpolation.

The spatial distribution of sample numbers over each radiosonde station at four different synoptic times (0000 UTC, 0600 UTC, 1200 UTC, 1800 UTC) is presented in Figure Fig. 1. It is noticeable that the radiosonde stations over Europe, the U.S., China, and Australia have an unprecedented rich geographic a spatially even coverage.

设置了格式: 非突出显示

设置了格式: 非突出显示

Furthermore, the radiosonde measurements~~observation~~ over China and the U.S. ~~has a~~have a fair temporal continuity at 0000 UTC and 1200 UTC, with a total sample ~~number~~size reaching up to as large as 3000 for each station. In comparison, the stations are poorly distributed over regions or countries such as southern America, the Pacific islands, Russia, the Middle East, India, and Africa.

2.2 ERA5 and GLDAS

ERA5 is the latest version of ECMWF reanalysis, benefiting from a decade of developments in model physics, core dynamics, and data assimilation (Hersbach et al., 2020). The PBLH product is resolved by the ERA5 reanalysis on a 1440×721 longitude/latitude grid, with a spatial resolution of 0.25°×0.25° and a temporal resolution of 1 hour, which is realistically simulated by the bulk Richardson number method. In addition, the parameters, such as the lower tropospheric stability (LTS), the standard deviation of digital elevation model (SDDEM), 10-m surface wind speed, 2-m air temperature, and 2-m pressure, are either computed or directly extracted from ERA5 reanalysis. LTS is defined as the difference in potential temperature between ~~the~~ 700 ~~hPa level~~ and 1000 hPa (Guo et al., 2016). As a result, a total of six parameters were obtained ~~based on~~from ERA5 reanalysis.

The land property parameters were taken from ~~NASA Global Land Data Assimilation System (~~GLDAS~~)~~, which include downward short-wave radiation (DSWR), downward long-wave radiation (DLWR), surface heat net flux (SHF), surface latent heat net flux (LHF), evapotranspiration, transpiration, soil moistures in 0–10 cm, 10–40 cm, 40–100 cm, and 100–200 cm, and total precipitation ~~rate~~amount. Totally, 11 parameters were extracted from the GLDAS product. GLDAS has a temporal resolution of 3 hours and the same spatial resolution as that of ERA5 reanalysis. However, GLDAS has no data over Antarctica. It should be noted that t~~T~~here exists a 0.125° lag between the ~~-~~start latitude and longitude of GLDAS and ~~are 0.125° lag of~~ those of ERA5 and therefore, the latitude and longitude of GLDAS ~~will~~ were~~be~~ minus 0.125°~~,~~ have to be used to match with ERA5 reanalysis.

~~The collocation procedure between grid product (ERA5 and GLDAS) and radiosonde follows~~ According to the methods proposed by Guo et al. (2021), the collocation procedures between the grid products from ERA5 and GLDAS and station-based radiosonde observations ~~which can~~ were mainly ~~be~~ implemented as follows. (1) The grid should contain the radiosonde station. (2) The UTC time (hour) of grid product and radiosonde stay the same.

2.3 PBLH determination by using bulk Richardson number method

The bulk Richardson number (Ri) is widely used for the climatological study of PBLH from radiosonde measurements thanks to its applicability and reliability for all atmospheric conditions (Anderson 2009; Seidel *et al.*, 2012). Ri, ~~as~~ a good indicator of turbulence and thermodynamic stability, is calculated as the ratio of turbulence due to buoyancy to that due to mechanical shear, which is formulated as

$$\mathrm{Ri(z)} = \frac{\left(\frac{g}{\theta_{vs}}\right)(\theta_{vz}-\theta_{vs})z_{AG}}{(u_z-u_s)^2+(v_z-v_s)^2+(bu_*^2)} \quad (1)$$

where g is the gravitational acceleration, z_{AG} the AGL, θ_v the virtual potential temperature, u_* the surface friction velocity, u and v the horizontal wind component, and b the constant which is usually set to zero since friction velocity is much weaker compared with the horizontal wind (Seidel *et al.*, 2012). The subscripts of z and s denote the parameters at z height above ground and the ground level, respectively.

The critical value of Ri(z) can be used to identify a statically stable layer atop the PBL (Seibert et al., 2000), and it is commonly taken as 0.25. Meanwhile, PBLH estimates were found varying little by differing the input of critical values ($\mathrm{Ri} = 0.2; 0.25; 0.3$) (Guo et al., 2016). Therefore, the PBLH here is identified as the interpolated height where Ri(z) profile crosses the critical value of 0.25. The determined PBLH was set invalid in ~~these~~ the following two scenarios: (1) ~~the second level of~~ Ri(z) in Eq. (1) exceeds 0.25, where z is the second level of radiosonde measurement; (2) the estimated PBLH is extremely high (for instance, 10 km), and it could mistake free-tropospheric features.

3. Methodology

As shown in ~~Figure~~ Fig. 2, there exist discernable biases between PBLH retrieved from radiosonde (hereinafter referred to as $PBLH_{RS}$ ~~R~~) and PBLH determined from ERA5 reanalysis (hereinafter referred to as $PBLH_{ERA5}$ ~~E~~). The match procedures between $PBLH_{RS}$ and $PBLH_{ERA5}$ follow Guo et al. (2021). ~~According to 185 million sounding measurements (Fig.2a)~~Noticeably, the PBLH bias ($PBLH_{RS}$~~R~~ minus $PBLH_{ERA5}$ ~~E~~) is less dependent on years, with a mean bias of 95.7 m, indicative of a possible systematic PBLH underestimation of the ERA5 reanalysis. By contrast, the underestimation is around 137 m during the daytime (Guo et al., 2021), which is systematically larger than that during all days obtained in the present study. However, the bias is found varying with seasons and local solar times (LST). More precisely, the mean bias varies from 150 m in the March–April–May (MAM) to 64 m in the September–October–November (SON), and from 309 m at 1700 LST to 1.8 m at 0000 LST. Moreover, the standard deviation of bias greatly changes from 64 m at 0100 LST to 807 m at 1700 LST. The large uncertainty raised by $PBLH_{ERA5}$ ~~E~~ during the daytime motivated this study to establish a new PBLH dataset that would be more consistent with observations.

Previous studies indicate that t~~T~~he bias could be ~~statistically~~ physically attributed to the variables such as SDDEM and LTS (Guo et al., 2021). However, the potential correlations with other variables, including DLWR, DSWR, SHF, LHF, evapotranspiration, transpiration, total precipitation rate (TPR), soil moistures (SMs), as well as wind speed, pressure, and air temperature at the near surface, ~~has~~ have yet~~not~~ to be~~en~~ systematically investigated ~~discussed yet~~. ~~As shown in~~ Figure 3~~,~~ shows that the bias is positively correlated with SHF, transpiration, LTS, and 2-m near-surface temperature, with a correlation coefficient ranging from 0.39 to 0.9 based on 10 evenly split bins. However, these parameters could be independent. For instance, evapotranspiration is determined by surface features which include plant physiology, land cover, and soil moisture, and it is the most important non-radiative process

设置了格式: 下标

设置了格式: 下标

设置了格式: 下标

设置了格式: 下标

设置了格式: 下标

设置了格式: 下标

transmitting latent heat from the surface to the atmosphere (Cuxart and Boone, 2020). In addition, soil moisture probably contributes to decreases in the surface sensible flux locally (Basha and Ratnam, 2009). We further perform correlation analyses between the aforementioned variables and PBLH biases between radiosonde and ERA5 reanalysis, and the statistical results are shown in Table 2

~~The correlation coefficients and their confidence levels between PBLH bias between radiosonde and ERA5 reanalysis and these variables are presented in Table 2, according to all samples.~~

~~Based on these findings, I~~it is found that the PBLH bias is highly associated with the variations in land properties, near-surface meteorological conditions, terrain elevations, ~~lower tropospheric stabilities~~LTS, and solar cycles. Consequently, it is possible to predict the PBLH bias based on these potential influential variables. Once the spatially resolved bias is available, a bias corrected PBLH dataset, namely, a merged PBLH product (denoted as $PBLH_{merged}$ ~~-M~~ hereafter), can be acquired by perturbating $PBLH_{ERA5}$ ~~-E~~ with the addition of predicted bias. This process can be formulated as

$$PBLH_{merged}\ \cancel{PBLH-M} = PBLH_{bias} + PBLH_{ERA5}\cancel{PBLH-E} \qquad (2)$$

where $PBLH_{bias}$ denotes the PBLH bias to be predicted. Under this philosophy, here we established a data-driven $PBLH_{bias}$ prediction model, with abovementioned factors used as the potential input variables while the PBLH bias over radiosonde sites as the learning target. Considering the possible dependence on magnitude of $PBLH_{ERA5}$~~PBLH-E~~ and its corresponding LST, these two factors were also used as covariates in predicting PBLH bias.

After testing with several machine learning models, such as the ridge regression, the decision tree regressor, the support vector regressor, the multilayer perceptron regression, and random forest (RF), we find the latter method gives the most proper and robust prediction. Therefore, a RF regressor is established to give a prediction of $PBLH_{bias}$, and it can be described as

$$PBLH_{bias} = RF(DSWR, DLWR, LHF, SHF, \mathrm{EP}, \mathrm{TP}, \mathrm{SM10}, \mathrm{SM40}, \mathrm{SM100}, \mathrm{SM200}, \mathrm{TPR}, \mathrm{PBLHE}, \mathrm{LTS}, \mathrm{SDDEM}, \mathrm{NSP}, \mathrm{NST}, \mathrm{NSWS}, \mathrm{LST}) \qquad (3)$$

设置了格式: 下标

设置了格式: 下标

where the abbreviation RF represents the random forest regressor, and the other acronyms and abbreviations are listed in Table~~.~~ 2. In the RF model, the hyper-parameters of the maximum depth of the tree and the random state of the bootstrapping of the samples are compiled to 20 and 5 in this analysis, respectively. The dataset that contains the input array and the learning target is randomly divided into two parts, with 70% for training and 30% for validation. All the data from 2011–2021 were included in the model training stage. The following statistical metrics, including the mean squared error (MSE), root mean square error (RMSE), arithmetic mean, and arithmetic mean of the absolute difference, are applied to evaluate the performance of the prediction model.

4 Validation

Table 3a presents the prediction accuracy on the training and testing sets. Overall, the RMSE and arithmetic mean on the training subset are 243 and –0.2, respectively. In comparison, these two metrics are 370 and –2.8 on the testing subset, implying the presence of slight overfitting. To demonstrate the merit of $PBLH_{merged}$~~PBLH-M~~, we further compare the PBLH bias before and after merging. As illustrated in Fig.4a, the mean bias between $PBLH_{RS}$~~-R~~ and $PBLH_{merged}$ ~~PBLH-M~~ is −0.9 m, which is smaller than the bias between $PBLH_{RS}$~~-R~~ and $PBLH_{ERA5}$~~-E~~. In addition, the mean of absolute bias decreases from 260 m ($PBLH_{RS}$~~-R~~ minus $PBLH_{ERA5}$~~-E~~) to 168 m ($PBLH_{RS}$~~-R~~ minus $PBLH_{merged}$~~-M~~), and the standard derivation declines from 472 m to 241 m, as listed in Tab~~.~~le 3b. Moreover, the correlation coefficient between $PBLH_{RS}$~~-R~~ and $PBLH_{ERA5}$~~-E~~ is 0.59, and it increases to 0.92 between $PBLH_{RS}$~~-R~~ and $PBLH_{merged}$~~PBLH-M~~. More importantly, the bias between $PBLH_{RS}$~~-R~~ and $PBLH_{merged}$ ~~PBLH-M~~ during the daytime is dramatically decreased to 20 m, compared to the bias between $PBLH_{RS}$~~-R~~ and $PBLH_{ERA5}$ ~~PBLH-E~~ (300 m). These metrics clearly demonstrate a better accuracy of $PBLH_{merged}$ ~~PBLH-M~~ than $PBLH_{ERA5}$~~-E~~, indicative of the merit of correcting modeling biases in $PBLH_{ERA5}$~~-E~~.

设置了格式: 下标
设置了格式: 下标
设置了格式: 下标
设置了格式: 下标
设置了格式: 下标
设置了格式: 下标
设置了格式: 下标
设置了格式: 下标
设置了格式: 下标
设置了格式: 下标
设置了格式: 下标
设置了格式: 下标
设置了格式: 下标
设置了格式: 下标

Furthermore, the overview of PBLH bias (PBLH$_{RS}$~~-R~~ minus PBLH$_{merged}$~~-M~~) in terms of spatial variation, and the seasonal variations over the four regions of interest are presented in ~~Figure~~ Fig. 5. As compared to the finding in Guo et al. (2021), the bias dramatically decreases to dozens of meters for all the stations (Fig. 5d), many of which slightly overestimate PBLH. More specifically, the PBLH over East Asia is overestimated by around 6 m (Fig.5f), whereas it is underestimated by around 1 m over Northern America (Fig. 5a). Based on the bias with near-global coverage, we could infer that the merged model gives a more realistic PBLH estimate.

Intensive radiosonde observation is conducted across China in boral summer season at 0600 UTC (1400 Beijing Time) when the PBL is fully developed (Zhang et al., 2018). In addition to the overall near-global spatial distribution, a deeper investigation of PBLH$_{merged}$~~-M~~ across China at 0600 UTC is presented in ~~Figure~~ Fig. 6. The spatial distribution of PBLH$_{merged}$~~-M~~ exhibits a pronounced "Northwest High Southeast Low" spatial pattern (~~Figure~~ Fig. 6a), which generally agrees with Zhang et al. (2018). The correlation coefficient between PBLH$_{merged}$~~-M~~ and PBLH$_{RS}$~~-R~~ is as high as 0.99, indicating their extreme consistencies in terms of spatial variations. The annual variations in PBLH$_{merged}$~~-M~~, PBLH$_{RS}$~~-R~~, and PBLH$_{ERA5}$~~-E~~ follow a similar trend, achieving a maximum in 2013 and a minimum in 2019 (Fig. 6b). The variations in PBLH$_{merged}$~~-M~~ and PBLH$_{RS}$~~-R~~ are rather close to each other. However, PBLH$_{ERA5}$~~-E~~ creates a different temporal variation, and it is systematically underestimated, compared to PBLH$_{RS}$~~-R~~.

As a good case in point for the comparison of fine structures, we show the diurnal variation of PBLH$_{merged}$ ~~PBLH-M~~ and PBLH$_{RS}$~~-R~~ at 0600 UTC over three stations in ~~Figure~~ Fig. 7. Three sites, including one in northwestern China where the highest PBLH is usually obtained, one in northern China where the most intensive observations can be found, and one in southern China where the lowest PBLH can be detected. The diurnal variations of PBLH$_{merged}$ ~~PBLH-M~~ and PBLH$_{RS}$~~-R~~ are strongly correlated with the lowest correlation of 0.88 (Fig.7d). From Figs. 5-7, we can observe that the spatial-temporal variations of PBLH$_{merged}$ ~~PBLH-M~~ and PBLH$_{RS}$~~-R~~ are in good agreement.

设置了格式: 下标
设置了格式: 下标
设置了格式: 下标
设置了格式: 下标
设置了格式: 下标
设置了格式: 下标
设置了格式: 下标
设置了格式: 下标
设置了格式: 下标
设置了格式: 下标
设置了格式: 下标
设置了格式: 下标
设置了格式: 下标
设置了格式: 下标
设置了格式: 下标
设置了格式: 下标
设置了格式: 下标
设置了格式: 下标
设置了格式: 下标

5 Merged continental planetary boundary layer height

The climatological mean of $PBLH_{merged}$ ~~PBLH-M~~ in four seasons at 0000~~,~~ ~~0600,1200,~~ and 12~~8~~00 UTCs during the years from 2011 to 2021 is illustrated in ~~Figure~~ Fig. 8, and the $PBLH_{RS}$ ~~-R~~ at the same UTC and in the same season are overlaid as filled circles. At all UTCs and in all seasons the $PBLH_{merged}$ ~~PBLH-M~~ is considerably high during the daytime and reaches a maximum of around 2 km, especially in the afternoon, as compared to the nighttime. In addition, $PBLH_{merged}$ ~~PBLH-M~~ experiences a noticeable seasonal variation. For instance, over Australia, the $PBLH_{ERA5}$ ~~-E~~ in SON and December–January–February (DJF) seasons is about 400 m larger than those of the other two seasons (Fig.8a–d), and vice versa in the Northern Hemisphere. Moreover, we can observe that $PBLH_{merged}$ ~~PBLH-M~~ has a clear latitude- and elevation-dependent. It decreases from approximately 2 km at low and middle latitudes to around 0.8 km at high latitudes during the daytime. At similar latitudes, the $PBLH_{merged}$ ~~-M~~ over terrain with a high elevation could be substantially larger than that with a low elevation. For example, in DJF~~MAM~~ season and at 00~~18~~00 UTC the $PBLH_{ERA5}$ ~~-E~~ over the Andes Mountain is about 0.4~~6~~ km higher than that over the surrounding flat region (Fig. 8d~~m~~). In a short conclusion, the spatial-temporal variability of the $PBLH_{merged}$ ~~PBLH-M~~ is inevitably associated with local times, seasons, latitudes, terrain elevations, and hemispheres.

In general, $PBLH_{merged}$ ~~PBLH-M~~ is remarkably consistent with $PBLH_{RS}$ in terms of seasonal variation and diurnal cycle, especially at 0000 UTC and 1200 UTC when the radiosonde measurement is comparatively sufficient. These findings suggest that the $PBLH_{merged}$ ~~PBLH-M~~ could adequately resolve the climatological variation of PBLH.

The difference in $PBLH_{merged}$ ~~PBLH-M~~ and $PBLH_{ERA5}$ ~~-E~~ during the years 2011–2021 at four typical times is further illustrated in ~~Figure~~ Fig. 9. Compared to $PBLH_{ERA5}$ ~~-E~~, the $PBLH_{merged}$ ~~PBLH-M~~ is overall overestimated, with a mean overestimation of approximately 90 m. The overestimation appears very close to the difference in

设置了格式: 下标
设置了格式: 下标
设置了格式: 下标
设置了格式: 非突出显示
设置了格式: 非突出显示
设置了格式: 下标
设置了格式: 非突出显示
设置了格式: 非突出显示
设置了格式: 下标
设置了格式: 下标

$PBLH_{RS}$~~-R~~ and $PBLH_{ERA5}$~~-E~~. The overestimation over North America at 0000 UTC, over East Asia and South Asia at 1200 UTC, and over Africa at 1800 UTC can be as high as 500 m. However, PBLH over some areas, such as the Middle East at 0600 UTC and the Western United States at 1800 UTC, is slightly underestimated by around 200 m.

6 Conclusions and summary

The general underestimation of PBLH by reanalysis dataset, especially during the daytime, motivates the present analysis to generate a merged long-term high-resolution seamless continental PBLH dataset (i.e., $PBLH_{merged}$~~PBLH-M~~) by integrating multi-modal data products, which includes 185 million high-resolution radiosondes from the years 2011 to 2021, ERA5 reanalysis, and GLDAS product. The $PBLH_{merged}$~~-M~~ generated in this study has a horizontal resolution of 0.25°×0.25° and a temporal resolution of 3 hours, identical to $PBLH_{ERA5}$~~-E~~, but with much higher data accuracy.

Compared to the $PBLH_{RS}$~~-R~~, the ~~PBLH-M~~ $PBLH_{merged}$ is overestimated by around –0.9 m, which is considerably smaller than the bias between $PBLH_{RS}$~~-R~~ and $PBLH_{ERA5}$~~-E~~ (95.7 m). During the daytime, the mean and the standard derivation of bias are remarkedly decreased from 300 m and 600 m ($PBLH_{RS}$~~-R~~ minus $PBLH_{ERA5}$~~-E~~) to 20 m and 300 m ($PBLH_{RS}$~~-R~~ minus $PBLH_{merged}$~~PBLH-M~~), respectively. In addition, the climatological variation of the merged PBLH dataset is highly correlated with $PBLH_{RS}$~~-R~~, both in magnitude and spatial-temporal variation. Moreover, the climatological mean of continental $PBLH_{merged}$~~-M~~ is around 90 m higher than that of $PBLH_{ERA5}$~~-E~~, which is quantitatively consistent with the comparison result of $PBLH_{RS}$~~-R~~ and $PBLH_{ERA5}$~~-E~~. Overall, the merged dataset closely agrees with the radiosonde-derived PBLH in terms of magnitude and spatial-temporal variation.

In conclusion, the $PBLH_{merged}$ ~~PBLH-M~~ dataset is outstanding in terms of both spatiotemporal coverage and good accuracy. This dataset could be of importance for advancing our understanding of the PBL processes involved in air quality prediction, weather forecast, and climate projection under global warming. In the future, with more

设置了格式: 下标
设置了格式: 下标
设置了格式: 下标
设置了格式: 下标
设置了格式: 下标
设置了格式: 下标
设置了格式: 下标
设置了格式: 下标
设置了格式: 下标
设置了格式: 下标
设置了格式: 下标
设置了格式: 下标
设置了格式: 下标
设置了格式: 下标
设置了格式: 下标

dataset available over the ocean, the global seamless PBLH dataset is warranted, and this needs more field campaigns to be deployed over the open ocean or islands in the ocean in which more intensive radiosonde balloons are launched. Besides, it is imperative to improve the observational capability of satellite-based instruments in characterizing the temperature and humidity profiles in the PBL, which no doubt helps fill the gaps of atmospheric sounding over the ocean.

Author contributions

JG and FH conceptualized this study. JG and JZ carried out the dataset production with comments from other co-authors. JG, JZ and JS drafted the first manuscript, and JS, KB, and RL further revised it. JS established ~~contributed to~~ the model ~~establish~~ and its optimization. All authors contributed to the discussion of result interpretation and helped finalized the submission.

Competing interests

The contact author has declared that neither they nor their co-authors have any competing interests.

Financial support

This study is jointly supported by the Natural Science Foundation of China under grants U2142209 and 62101203, the Hubei Provincial Natural Science Foundation of China under grant KZ22Z3021,~~and~~ the Fundamental Research Funds for the Central Universities, China University of Geosciences (Wuhan) under ~~(~~grant~~no.~~ 162301192698~~)~~, the Fundamental Research Funds for the Central Universities, Huazhong Agricultural University under grant 2662021XXQD002, the Chinese Academy of Sciences under grant GXDA20040502, and Chinese Academy of Meteorological Sciences under grant 2021KJ029.

Data availability

The merged PBLH dataset and the related codes can be accessed at https://doi.org/10.5281/zenodo.6498004 (Guo et al., 2022).

ERA5 data is publicly accessible at https://cds.climate.copernicus.eu/#!/search?text=ERA5&type=dataset (ECMWF, 2019). NASA GLDAS can be accessed at: https://disc.gsfc.nasa.gov/datasets/GLDAS_NOAH025_3H_2.1/summary?keywords=GLDAS (NASA, 2021).

References

Anderson, P. S: Measurement of Prandtl number as a function of Richardson number avoiding self-correlation, Boundary Layer Meteorol, 131, 345–362, https://doi.org/10.1007/s10546-009-9376-4, 2009.

Baklanov, A. A., Grisogono, B., Bornstein, R., Mahrt, L., Zilitinkevich, S. S., Taylor, P., Larsen, S.E., Rotach, M.W. and Fernando, H. J. S.: The nature, theory, and modeling of atmospheric planetary boundary layers, Bull Am Meteorol Soc, 92(2), 123–128, https://doi.org/10.1175/2010BAMS2797.1, 2011

Basha, G., and Ratnam, M. V.: Identification of atmospheric boundary layer height over a tropical station using high-resolution radiosonde refractivity profiles: Comparison with GPS radio occultation measurements, J. Geophys. Res. Atmos., 114(D16), https://doi.org/10.1029/2008JD011692, 2009.

Chan, K. M., and Wood, R.: The seasonal cycle of planetary boundary layer depth determined using COSMIC radio occultation data, J. Geophys. Res. Atmos., 118, 12 422–12 434, https://doi.org/10.1002/2013JD020147, 2013.

Cooper, D. I. and Eichinger, W. E.: Structure of the atmosphere in an urban planetary boundary layer from lidar and radiosonde observations, J. Geophys. Res. Atmos., 99(D11), 22937–22948, https://doi.org/10.1029/94JD01944, 1994.

Cuxart, J., and Boone A. A.: Evapotranspiration over Land from a Boundary-Layer Meteorology Perspective. Boundary Layer Meteorol., 177, 427–459, https://doi.org/10.1007/s10546-020-00550-9, 2020.

Davis, E. V., Rajeev, K., and Mishra, M.K.: Effect of clouds on the diurnal evolution of the atmospheric boundary-layer height over a tropical coastal station, Boundary Layer Meteorol., 175(1), 135–152, https://doi.org/10.1007/s10546-019-00497-6, 2020.

Davy, R., and Esau, I.: Differences in the efficacy of climate forcings explained by variations in atmospheric boundary layer depth, Nat. Commun., 7(1), 11690. https://doi.org/10.1038/ncomms11690, 2016.

de Arruda Moreira, G., Guerrero-Rascado, J. L., Bravo-Aranda, J. A., Benavent-Oltra, J. A., Ortiz-Amezcua, P., Róman, R., Bedoya-Velásquez, A. E., Landulfo, E. and Alados-Arboledas, L.: Study of the planetary boundary layer by microwave radiometer, elastic lidar and Doppler lidar estimations in Southern Iberian Peninsula, Atmos Res., 213, 185–195, https://doi.org/10.1016/j.atmosres.2018.06.007, 2018.

Degrazia, G. A., D. Anfossi, J. C. Carvalho, C. Mangia, T. Tirabassi and Campos Velho, H. F.: Turbulence parameterisation for PBL dispersion models in all stability conditions, Atmos. Environ., 34(21), 3575–3583, https://doi.org/10.1016/S1352-2310(00)00116-3, 2000.

Ding, F., Iredell, L., Theobald, M., Wei, J., and Meyer, D.: PBL height from AIRS, GPS RO, and MERRA-2 products in NASA GES DISC and their 10-year seasonal mean intercomparison, Earth Space Sci., 8, e2021EA001859, https://doi.org/10.1029/2021EA001859, 2021.

Dirmeyer, P. A., Wang, Z., Mbuh, M. J. and Norton, H. E.: Intensified land surface control on boundary layer growth in a changing climate, Geophys. Res. Lett., 41(4), 1290–1294, https://doi.org/10.1002/2013GL058826, 2014.

ECMWF.: ERA5 reanalysis [data set], Retrieved from https://cds.climate.copernicus.eu/#!/search?text=ERA5&type=dataset, 2019.

Edson, J. B., Jampana, V., Weller, R. A., Bigorre, S. P., Plueddemann, A. J., Fairall, C. W., Miller, S. D., Mahrt, L., Vickers, D., and Hersbach, H.: On the Exchange of Momentum over the Open Ocean, J Phys Oceanogr., 43(8), 1589–1610, https://doi.org/10.1175/JPO-D-12-0173.1, 2013.

Esau, I., and Zilitinkevich, S.: On the role of the planetary boundary layer depth in the climate system. Adv. Sci. Res., 4, 63, https://doi.org/10.5194/asr-4-63-2010, 2010.

Guo, J., Li, Y., Cohen, J. B., Li, J., Chen, D., Xu, H., Liu, L., Yin, J., Hu, K., and Zhai. P.: Shift in the temporal trend of boundary layer height in China using long-term (1979–2016) radiosonde data, Geophys. Res. Lett., 46, 6080–6089, https://doi.org/10.1029/2019GL082666, 2019.

Guo, J., Miao, Y., Zhang, Y., Liu, H., Li, Z., Zhang, W., He, J., Lou, M., Yan, Y., Bian, L., and Zhai, P.: The climatology of planetary boundary layer height in China derived from radiosonde and reanalysis data, Atmos. Chem. Phys., 16, 13309–13319, https://doi.org/10.5194/acp-16-13309-2016, 2016.

Guo, J., Zhang, J., Yang, K., Liao, H., Zhang, S., Huang, K., Lv, Y., Shao, J., Yu, T., Tong, B., Li, J., Su, T., Yim, S. H. L., Stoffelen, A., Zhai, P., and Xu, X.: Investigation of near-global daytime boundary layer height using high-resolution radiosondes: first results and comparison with ERA5, MERRA-2, JRA-55, and NCEP-2 reanalyses, Atmos. Chem. Phys., 21, 17079–17097, https://doi.org/10.5194/acp-21-17079-2021, 2021.

Guo, J., Zhang, J., Shao., J.: A Harmonized Global Continental High-resolution Planetary Boundary Layer Height Dataset Covering 2017-2021 [data set], https://zenodo.org/record/6498004, 2022.

Hennemuth, B., and Lammert, A.: Determination of the atmospheric boundary layer height from radiosonde and lidar backscatter, Boundary Layer Meteorol., 120(1), 181–200, https://doi.org/10.1007/s10546-005-9035-3, 2006.

Hersbach, H., Bell, B., Berrisford, P., Hirahara, S., Horányi, A., Muñoz-Sabater, J., Nicolas, J., Peubey, C., Radu, R., Schepers, D. and Simmons, A.: The ERA5 global reanalysis, Q. J. R. Meteorol. Soc., 146(730), 1999–2049, https://doi.org/10.1002/qj.3803, 2020.

Holzworth, G. C.: Estimates of mean maximum mixing depths in the contiguous United States, Mon. Wea. Rev., 92, 235–242, https://doi.org/10.1175/1520-0493(1964)092,0235: EOMMMD.2.3.CO;2, 1964.

Hu, X. M., Nielsen-Gammon, J. W. and Zhang, F.: Evaluation of three planetary boundary layer schemes in the WRF model, J Appl Meteorol Climatol., 49(9), 1831–1844, https://doi.org/10.1175/2010JAMC2432.1, 2010.

Lammert, A., and Bösenberg, J.: Determination of the con- vective boundary-layer height with laser remote sensing, Bound.-Layer Meteor., 119, 159–170, https://doi.org/10.1007/ s10546-005-9020-x, 2006.

Li, Q., Zhang, H., Cai, X. et al.: The impacts of the atmospheric boundary layer on regional haze in North China, npj Clim Atmos Sci., 4(1), 1–10. https://doi.org/10.1038/s41612-021-00165-y, 2021.

Li, Z., Guo, J., Ding, A., Liao, H., Liu, J., Sun, Y., Wang, T., Xue, H., Zhang, H. and Zhu, B.: Aerosol and boundary-layer interactions and impact on air quality. Natl. Sci. Rev., 4(6), 810–833, https://doi.org/10.1093/nsr/nwx117, 2017.

Liu, B., Y. Ma, J. Guo, W. Gong, Y. Zhang, F. Mao, J. Li, X. Guo, and Shi, Y.: Boundary layer heights as derived from ground-based radar wind profiler in Beijing, IEEE Trans. Geosci. Remote Sens. 57(10), 8095–8104, https://doi.org/10.1109/TGRS.2019.2918301, 2019.

Lou, M., J. Guo, L. Wang, H. Xu, D. Chen, Y. Miao, Y. Lv, Y. Li, X. Guo, S. Ma, and Li, J.: On the relationship between aerosol and boundary layer height in summer in China under different thermodynamic conditions. Earth Space Sci., 6(5), 887–901, https://doi.org/10.1029/2019EA000620, 2019.

McGrath-Spangler, E. L., and Denning, A. S.: Estimates of North American summertime planetary boundary layer depths derived from space-borne lidar. J. Geophys. Res., 117, D15101, https://doi.org/10.1029/2012JD017615, 2012.

Min, M., Bai, C., Guo, J., Sun, F., Liu, C., Wang, F., Xu, H., Tang, S., Li, B., Di, D. and Dong, L.: Estimating summertime precipitation from Himawari-8 and global forecast system based on machine learning, IEEE Trans Geosci Remote Sens., 57(5), 2557–2570, https://doi.org/10.1109/TGRS.2018.2874950, 2018.

NASA.: Global Land Data Assimilation System [data set], Retrieved from https://disc.gsfc.nasa.gov/datasets/GLDAS_CLSM025_DA1_D_2.2/summary?keywords=GLDAS, 2021.

Petäjä, T., Järvi, L., Kerminen, VM. et al.: Enhanced air pollution via aerosol-boundary layer feedback in China, Sci. Rep., 6, 18998. https://doi.org/10.1038/srep18998, 2016.

Rodell, M., Houser, P. R., Jambor, U. E. A., et al.: The global land data assimilation system. Bull. Am. Meteorol. Soc., 85(3), 381–394, https://doi.org/10.1175/BAMS-85-3-381, 2004.

Saha, S., Sharma, S., Kumar, K.N., Kumar, P., Lal, S. and Kamat, D.: Investigation of atmospheric boundary layer characteristics using ceilometer lidar, COSMIC GPS RO satellite, radiosonde and ERA-5 reanalysis dataset over Western Indian region, Atmos Res., 268, 105999, https://doi.org/10.1016/j.atmosres.2021.105999, 2022.

Seibert, P., Beyrich, F., Gryning, S.-E., Joffre, S., Rasmussen, A., and Tercier, P.: Review and intercomparison of operational methods for the determination of the mixing height, Atmos. Environ., 34, 1001–1027, https://doi.org/10.1016/S1352-2310(99)00349-0, 2000.

Seidel, D. J., Ao, C. O., and Li, K.: Estimating climatological planetary boundary layer heights from radiosonde observations: Comparison of methods and uncertainty analysis, J. Geophys. Res. Atmos., 115(D16). https://doi.org/10.1029/2009JD013680, 2010.

Seidel, D. J., Zhang, Y., Beljaars, A., Golaz, J. C., Jacobson, A.R. and Medeiros, B.: 2012. Climatology of the planetary boundary layer over the continental United States and Europe, J. Geophys. Res. Atmos., 117(D17), https://doi.org/10.1029/2012JD018143, 2012.

Stull, R. B..: An Introduction to Boundary Layer Meteorology. Kluwer Academic, 666 pp, 1988.

Su, T., Li, Z., and Kahn, R.: Relationships between the planetary boundary layer height and surface pollutants derived from lidar observations over China: regional pattern and influencing factors, Atmos. Chem. Phys., 18, 15921–15935, https://doi.org/10.5194/acp-18-15921-2018, 2018.

Teixeira, J., Piepmeier, J. R., Nehrir, A. R., Ao, C. O., Chen, S. S., Clayson, C. A., Fridlind, A. M., Lebsock, M., Mc-Carty, W., Salmun, H., Santanello, J. A., Turner, D. D., Wang, Z., and Zeng, X.: Toward a global planetary boundary layer observing system: the NASA PBL incubation study team report, NASA PBL Incubation Study Team, 134 pp., available at: https://science.nasa.gov/science-red/s3fs-public/atoms/files/NASAPBLIncubationFinalReport.pdf, last access: 28 April 2022.

Wallace, J. M. and Hobbs, P. V: Atmospheric Science: An Introductory Survery, Academic Press, Burlington, MA., 2006.

Wang, X. and Wang, K.: Homogenized variability of radiosonde-derived atmospheric boundary layer height over the global land surface from 1973 to 2014, J. Clim., 29(19), 6893–6908, https://doi.org/10.1175/JCLI-D-15-0766.1, 2016.

Wang, Y., A. Khalizov, M. Levy, and Zhang, R.: New Directions: Light Absorbing Aerosols and Their Atmospheric Impacts, Atmos. Environ., 81, 713–715, https://doi.org/10.1016/j.atmosenv.2013.09.034, 2013.

Xu, Z., Chen, H., Guo, J., and Zhang, W.: Contrasting effect of soil moisture on the daytime boundary layer under different thermodynamic conditions in summer over China, Geophys Res. Lett., 48, e2020GL090989. https://doi.org/10.1029/2020GL090989, 2021.

Yang, X., Zhao, C., Guo, J., and Wang, Y.: Intensification of aerosol pollution associated with its feedback with surface solar radiation and winds in Beijing, J. Geophys. Res. Atmos., 121, 4093–4099, https://doi.org/10.1002/2015JD024645, 2016.

Zhang, J., Guo, J. P., Zhang, S. D., and Shao, J.: Inertia-gravity wave energy and instability drive turbulence: evidence from a near-global high-resolution radiosonde dataset, Clim. Dyn., 1–14, https://doi.org/10.1007/s00382-021-06075-2, 2022.

Zhang, W., Guo, J., Miao, Y., Liu, H., Song, Y., Fang, Z., He, J., Lou, M., Yan, Y., Li, Y., and Zhai, P.: On the summertime planetary boundary layer with different thermodynamic stability in China: A radiosonde perspective, J. Clim., 31(4), 1451–1465, https://doi.org/10.1175/JCLI-D-17-0231.1, 2018.

Table 1. Basic information of data used in the present study, including data source, the number of stations, vertical resolution, and the years with data curation.

Data source	**Number of station**	**Vertical resolution**	**Years**
CMA	120	5–8 m	2011–2021
NOAA	89	5 m	2011–2021
GRUAN	8	5 m	2011–2021
CEDA	12	10 m	2011–2021
University of Wyoming	125	5–10 m	2017–2021
German Deutscher Wetterdienst	14	10 m	2011–2021

Table 2. Summary of input parameters of machine learning algorithms, and the corresponding statistical metrics for their correlation analyses between ~~coefficient~~ with PBLH bias between radiosonde and ERA5 reanalysis, ~~and~~ including correlation coefficient and ~~its~~ confidence level.

Parameters	**Acronyms**	**Data sources**	**Correlation coefficient**	**Confidence level**
Downward shortwave radiation	DSWR	GLDAS	0.14	100%
Downward longwave radiation	DLWR	GLDAS	0.02	100%
Latent heat flux	LHF	GLDAS	0.14	100%
Sensible heat flux	SHF	GLDAS	0.10	100%
Evapotranspiration	EP	GLDAS	0.14	100%
Transpiration	TP	GLDAS	-0.02	100%
Soil moisture 0-10cm	SM10	GLDAS	-0.04	100%
Soil moisture 10-40cm	SM40	GLDAS	-0.03	100%
Soil moisture 40-100cm	SM100	GLDAS	-0.02	100%
Soil moisture 100-200cm	SM200	GLDAS	-0.03	100%
Total precipitation rate	TPR	GLDAS	-0.02	100%
Boundary layer height	$PBLH_{ERA5}$~~-E~~	ERA5	-0.10	100%
Lower tropospheric stability	LTS	ERA5	0.10	100%
Standard deviation of orography height	SDDEM	ERA5	0.06	100%
Near-surface pressure	NSP	ERA5	-0.11	100%
Near-surface temperature	NST	ERA5	0.05	100%
Near-surface wind speed	NSWS	ERA5	-0.08	100%
Local solar time	LST	-	0.17	100%

设置了格式: 下标

Table 3. Basic information on evaluation indices. MSE, mean squared error; RMSE, root mean square error; ABSmean, mean of the absolute bias; STD, standard derivation; RMS, root mean square.

(a) evaluation indices of the training set and test set

	MSE	RMSE	Mean	ABSmean
Train set	59176	243	–0.2	152
Predict set	136971	370	–2.8	204

(b) evaluation indices of PBLH bias

	Mean	ABSmean	STD	RMS
$PBLH_{RS}$ – $PBLH_{ERA5}$	95.7	260	472	481
$PBLH_{RS}$ – $PBLH_{merged}$	–0.9	168	241	287

设置了格式: 下标
设置了格式: 下标
设置了格式: 下标
设置了格式: 下标

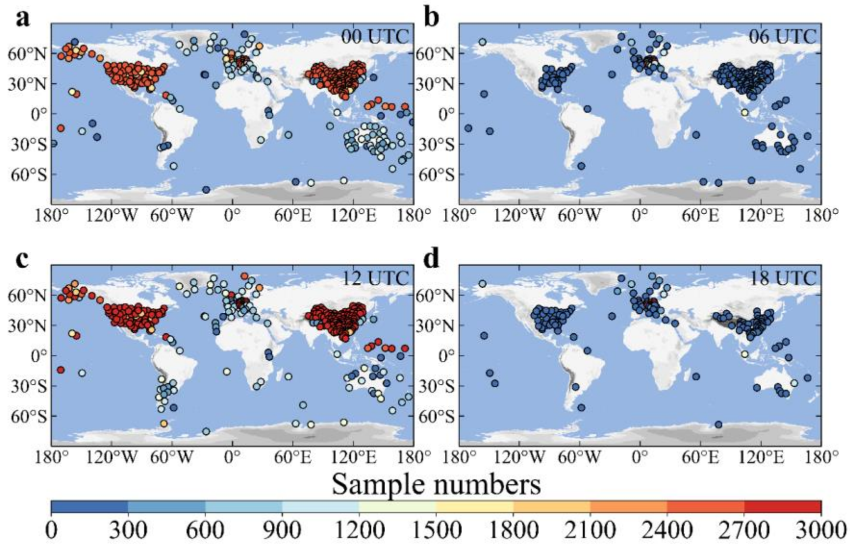

Figure 1. Spatial distribution of sample number (color circles) for each radiosonde station at 0000 (a), 0600 (b), 1200 (c), and 1800 UTC from the years 2011 to 2021. Stations with less than 10 samples are not indicated.

665 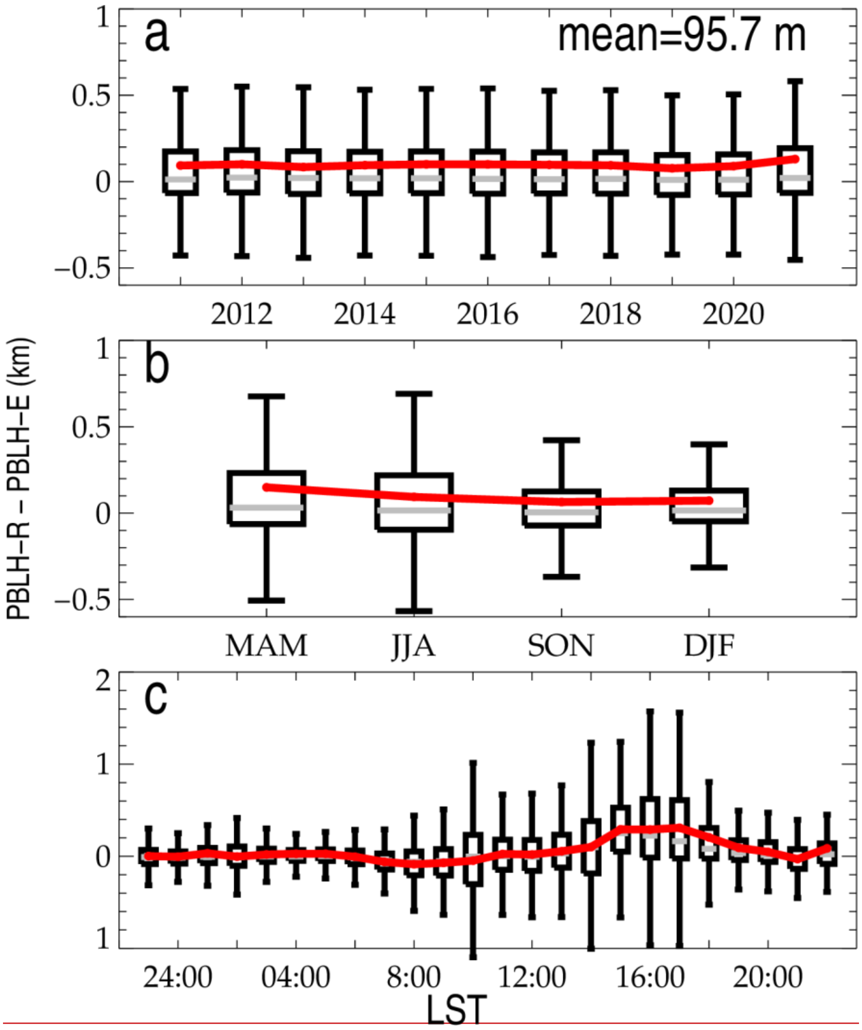
a
mean=95.7 m
1
0.5
0
−0.5
2012
2014
2016
2018
2020
b
PBLH−R − PBLH−E (km)
MAM
JJA
SON
DJF
c
2
24:00
04:00
8:00
12:00
16:00
20:00
LST

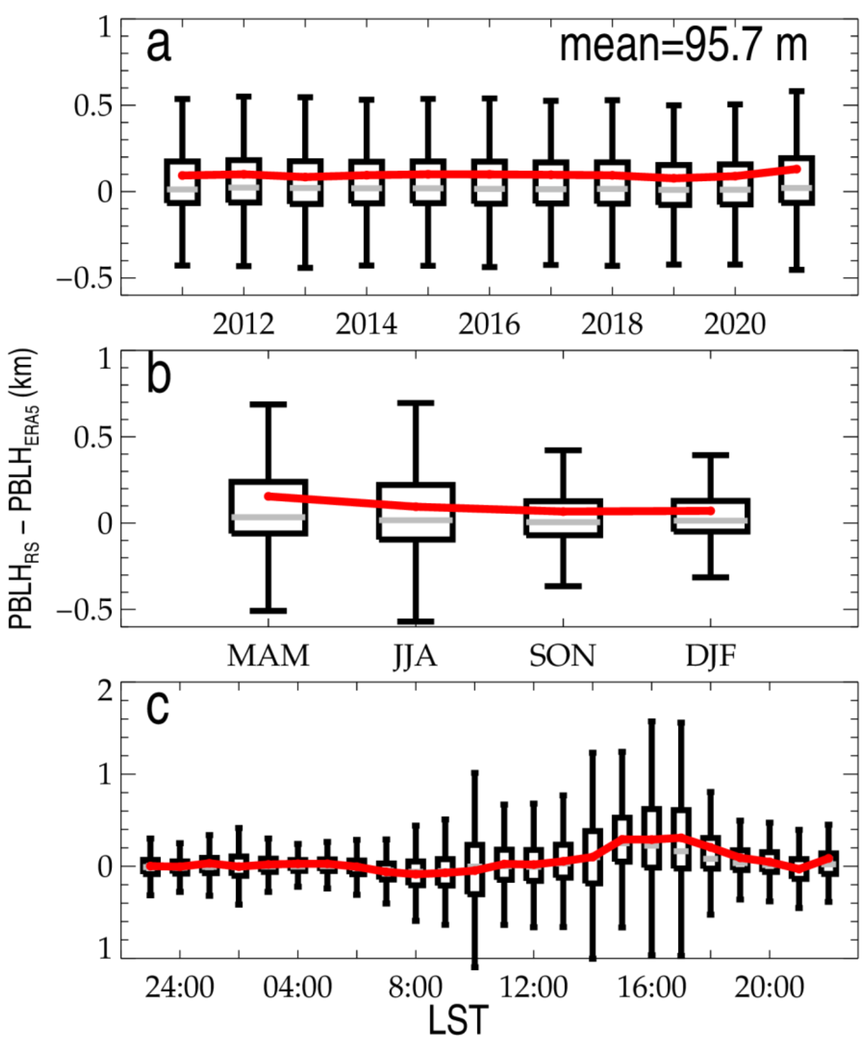

Figure 2. Evolution of the difference between PBLH$_{ERA5}$~~E~~ and PBLH$_{RS}$~~R~~ at various time scales: different years (a), different seasons (b), and at different local times (c). MAM, March–April–May; JJA, June–July– August; SON, September–October–November; DJF, December–January–February. The mean bias is labelled in the upper right corner of panel (a). Note that the southern hemisphere DJF (JJA) is combined with northern hemisphere JJA (DJF).

设置了格式: 下标

设置了格式: 下标

设置了格式: 字体: 小四, 非加粗

设置了格式: 字体: 小四, 非加粗

带格式的: 两端对齐

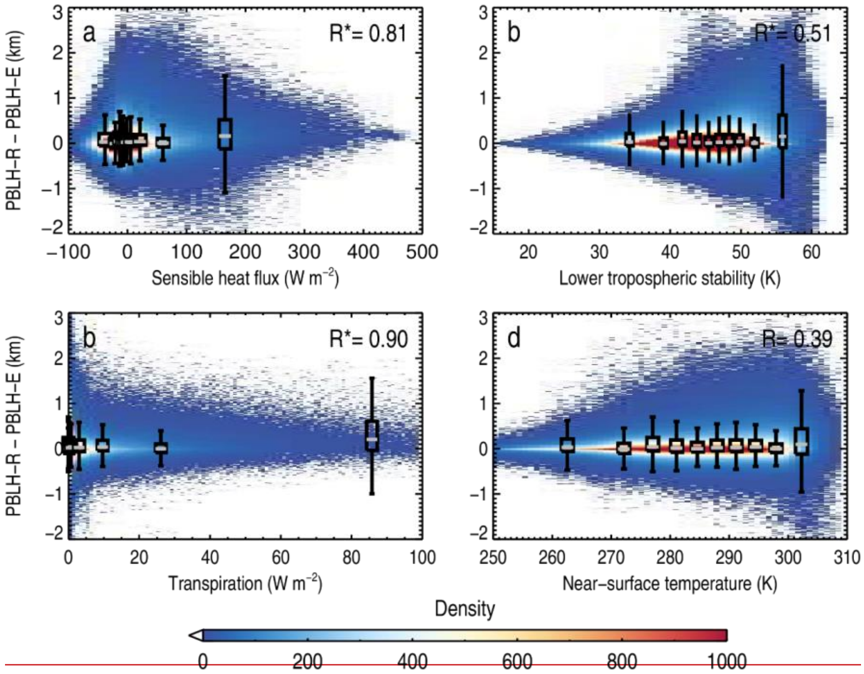
a
R* = 0.81
b
R* = 0.51
b
R* = 0.90
d
R = 0.39
PBLH−R − PBLH−E (km)
Sensible heat flux (W m−2)
Lower tropospheric stability (K)
Transpiration (W m−2)
Near−surface temperature (K)
Density
0
200
400
600
800
1000

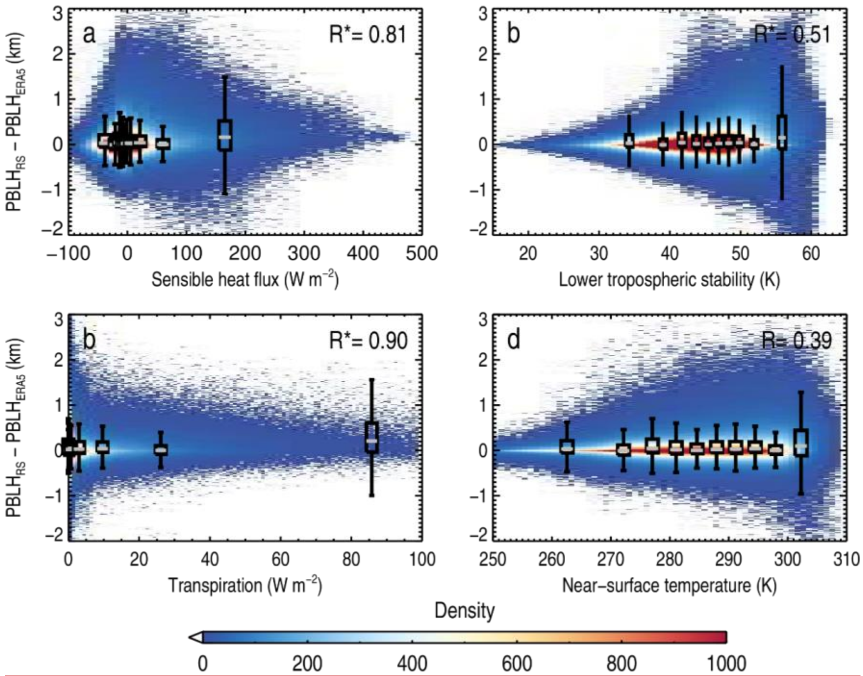
a
R* = 0.81
b
R* = 0.51
b
R* = 0.90
d
R = 0.39
PBLHRS − PBLHERA5 (km)
Sensible heat flux (W m−2)
Lower tropospheric stability (K)
Transpiration (W m−2)
Near−surface temperature (K)
Density
0
200
400
600
800
1000

Figure 3. The joint distribution of the difference in $PBLH_{RS}$~~-R~~ and $PBLH_{ERA5}$~~-E~~ and the surface sensible heat flux (a), the lower tropospheric stability (b), transpiration (c), and the near-surface temperature (d). The box-and-whisker plots in 10 evenly intervals are overlaid in each panel, and the correlation coefficients are marked in the upper right corner of each panel, wherein the star superscripts indicate that the values are statistically significant ($p<0.05$).

设置了格式: 下标

设置了格式: 下标

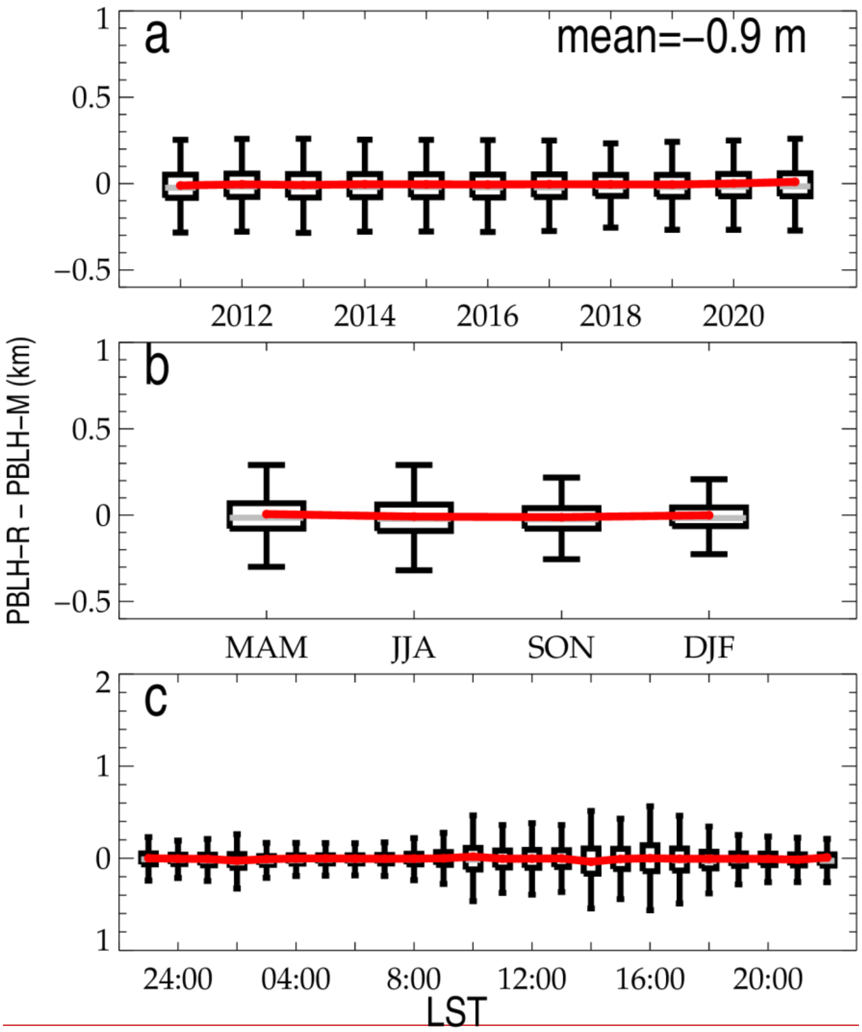
a
mean=−0.9 m
1
0.5
0
−0.5
2012
2014
2016
2018
2020
b
1
0.5
0
−0.5
MAM
JJA
SON
DJF
PBLH−R − PBLH−M (km)
c
2
1
0
1
24:00
04:00
8:00
12:00
16:00
20:00
LST

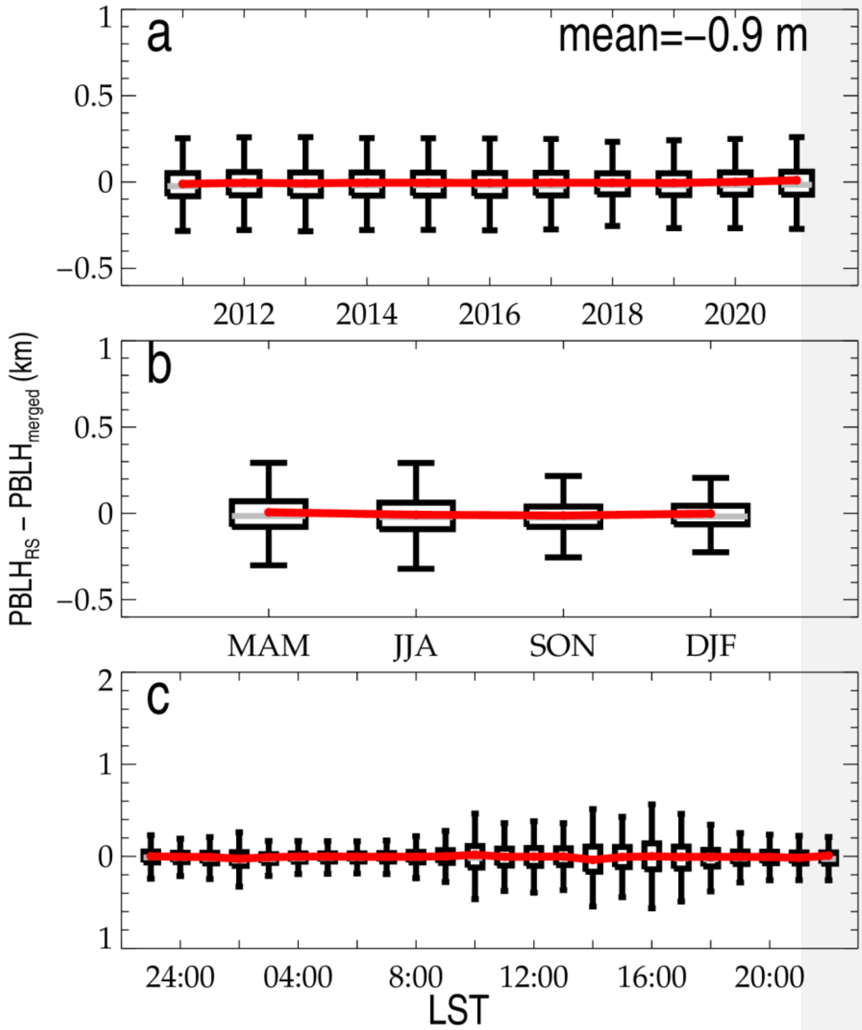

Figure 4. Similar to Figure 3, but for the difference between PBLH$_{RS}$ ~~R~~ and PBLH$_{merged}$ ~~M~~.

设置了格式: 下标

设置了格式: 下标

692 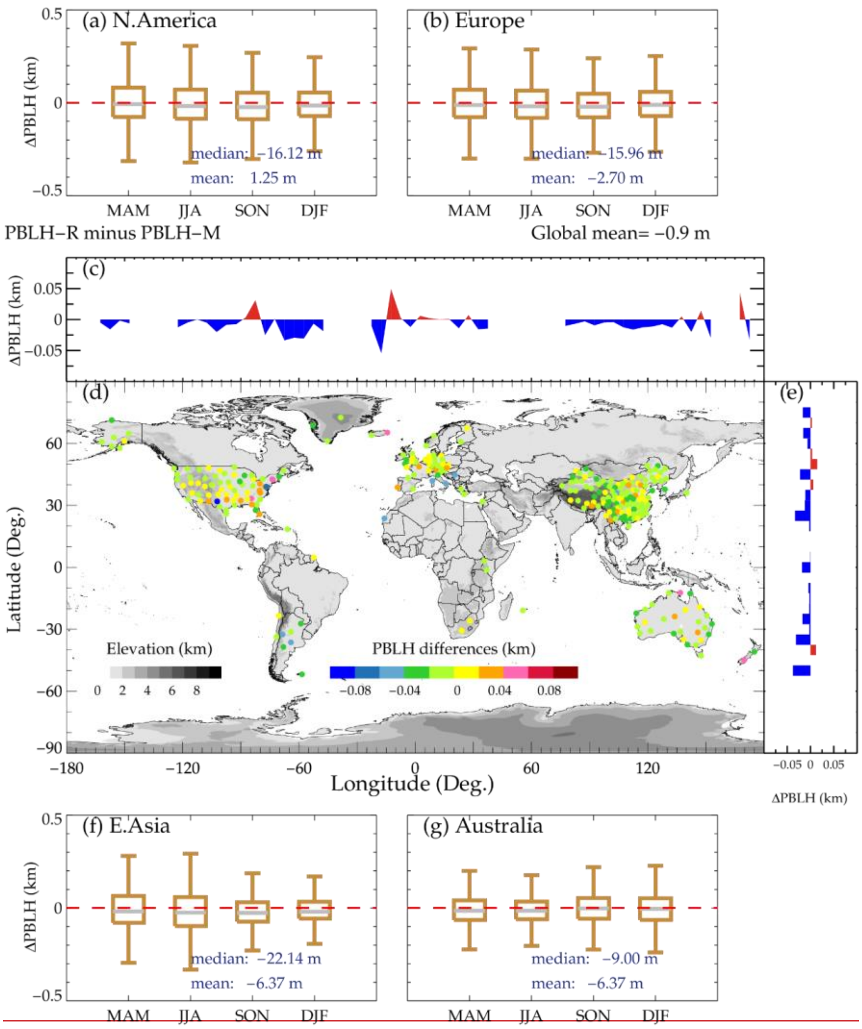
(a) N.America
ΔPBLH (km)
median: −16.12 m
mean: 1.25 m
MAM JJA SON DJF
(b) Europe
median: −15.96 m
mean: −2.70 m
PBLH−R minus PBLH−M
Global mean= −0.9 m
(c)
(d)
(e)
Latitude (Deg.)
Elevation (km)
PBLH differences (km)
Longitude (Deg.)
(f) E.Asia
median: −22.14 m
mean: −6.37 m
(g) Australia
median: −9.00 m
mean: −6.37 m

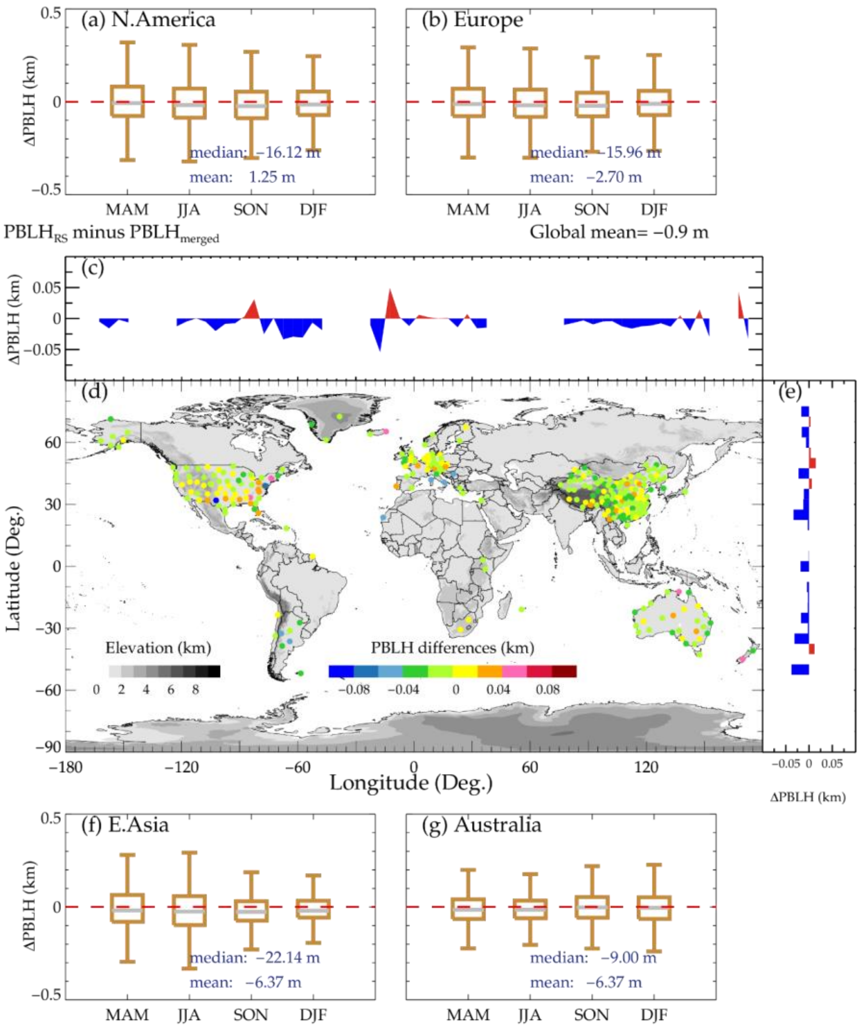

Figure 5. Spatial variations of PBLH differences between $PBLH_{RS}$ ~~R~~ and $PBLH_{merged}$ ~~M~~. (d) indicates the overall spatial distribution, and (c) and (d) illustrate its longitudinal and latitudinal variations. (a), (b), (f), (g) represent the seasonal variations over the four regions of interest, including North America, Europe, East Asia, and Australia. MAM, March–April–May; JJA, June–July—August; SON, September–October–November; DJF, December–January–February.

设置了格式: 下标

设置了格式: 下标

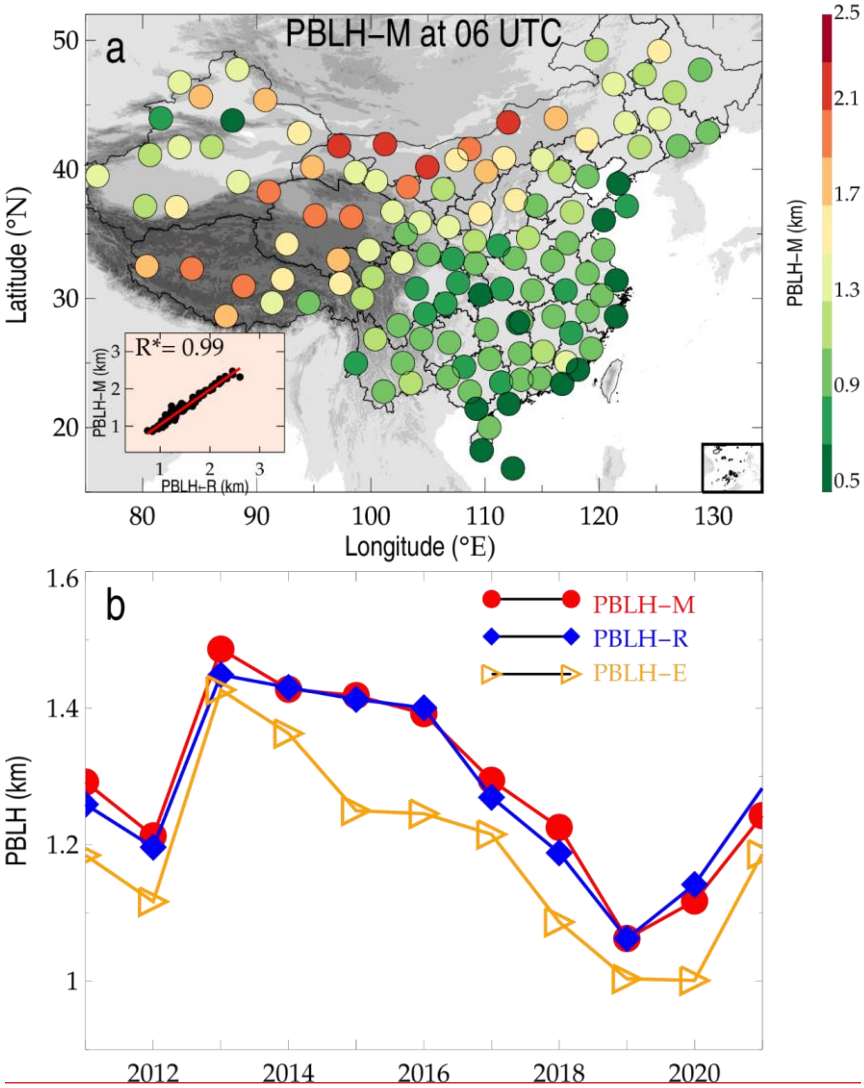
PBLH−M at 06 UTC
a
50
40
30
20
80
90
100
110
120
130
Latitude (°N)
Longitude (°E)
R*= 0.99
PBLH−M (km)
PBLH−R (km)
2.5
2.1
1.7
1.3
0.9
0.5
PBLH−M (km)
b
1.6
1.4
1.2
1
PBLH (km)
2012
2014
2016
2018
2020
PBLH−M
PBLH−R
PBLH−E

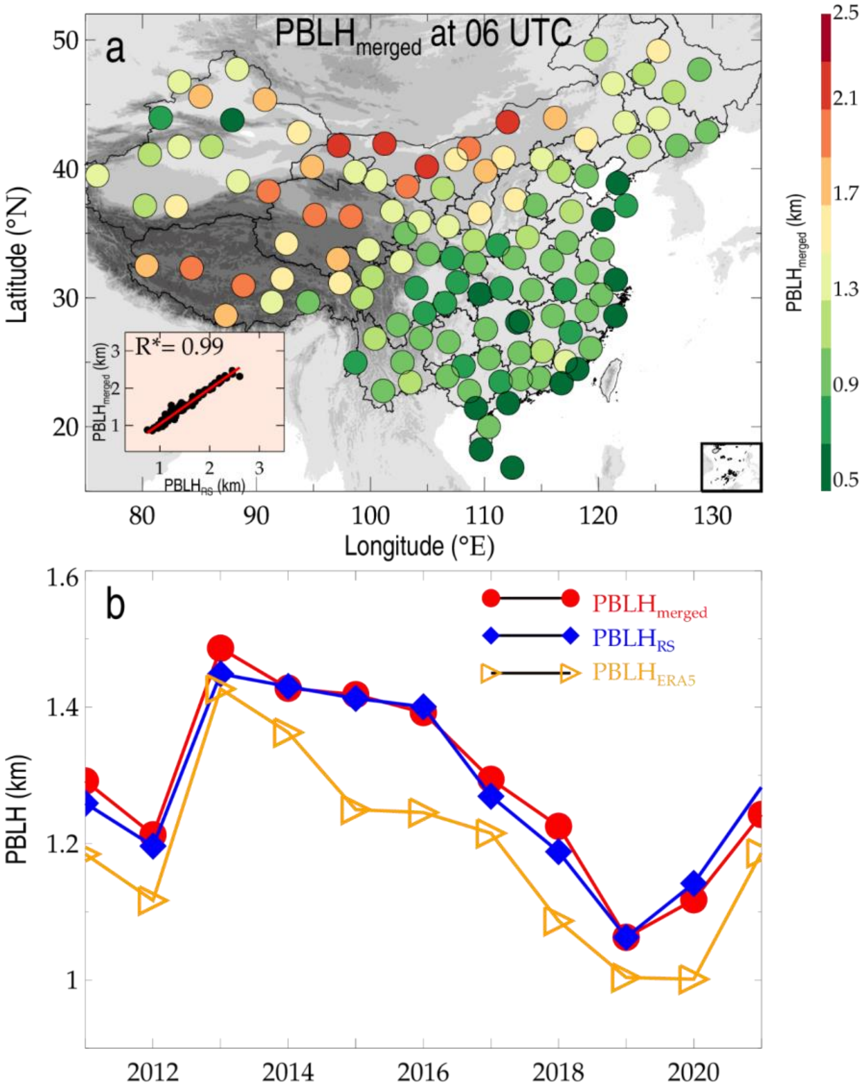

Figure 6. (a) Spatial distributions of the PBLH$_{merged}$ ~~M~~ at 0600 UTC across China for the years 2011 to 2021. The scatter plot in the left bottom of the panel illustrates the statistical correlation between PBLH$_{merged}$~~H M~~ and PBLH$_{RS}$ ~~R~~, where the star superscripts indicate that the values are statistically significant (p<0.05). Also shown are the temporal evolution of annual average PBLH$_{merged}$~~PBLH M~~, PBLH$_{RS}$ ~~R~~, and PBLH$_{ERA5}$ ~~E~~ during the period 2011 to 2021 (b).

设置了格式: 下标
设置了格式: 下标
设置了格式: 下标
设置了格式: 下标
设置了格式: 下标

708

设置了格式: 字体: (中文) +中文正文 (等线)

709 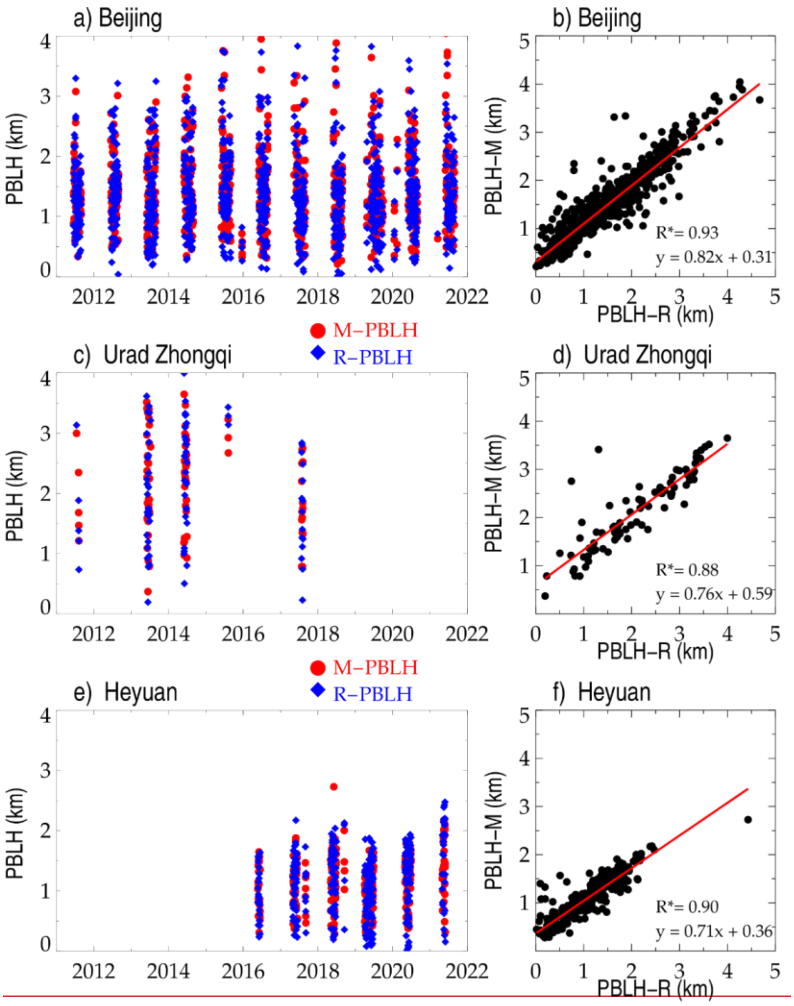
a) Beijing
PBLH (km)
b) Beijing
PBLH-M (km)
R*= 0.93
y = 0.82x + 0.31
PBLH-R (km)
M-PBLH
R-PBLH
c) Urad Zhongqi
d) Urad Zhongqi
R*= 0.88
y = 0.76x + 0.59
e) Heyuan
f) Heyuan
R*= 0.90
y = 0.71x + 0.36

带格式的: 居中

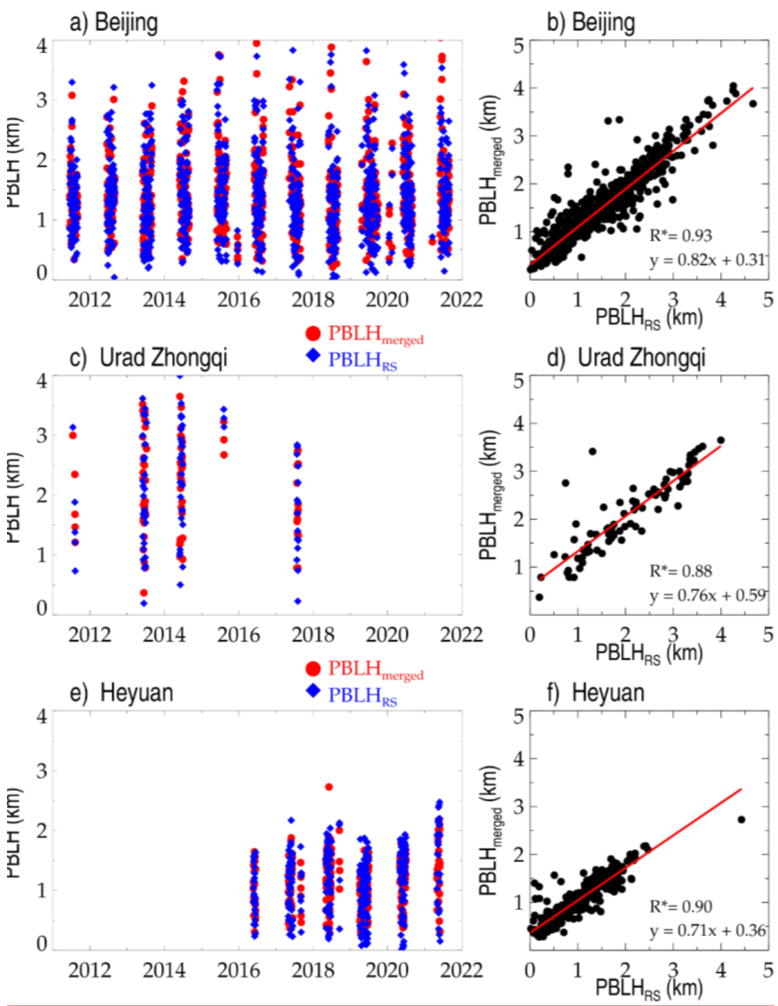

Figure 7. Temporal variations of $PBLH_{merged}$ ~~-M~~ (red) and $PBLH_{RS}$ ~~-R~~ (blue) at Beijing (39.8°N, 116.47°E) (a), the Urad Zhongqi station (41.3°N, 108.3°E) (b) in the Nei Monggol Autonomous Region, and (c) the Heyuan (23.7°N, 114.7°E) station in the Guangdong province. (b), (d), and (f) demonstrate the joint-distributions of $PBLH_{RS}$ ~~PBLH-R~~ and $PBLH_{merged}$ ~~-M~~, and correlation coefficients (R) and the fitted linear functions are given in the bottom right corner, where the star superscripts indicate that the values are statistically significant ($p<0.05$).

设置了格式: 下标

设置了格式: 下标

设置了格式: 下标

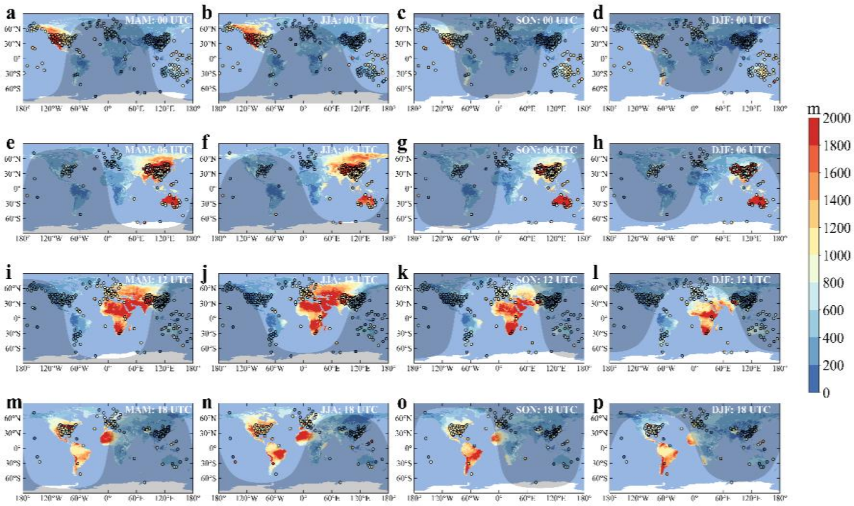

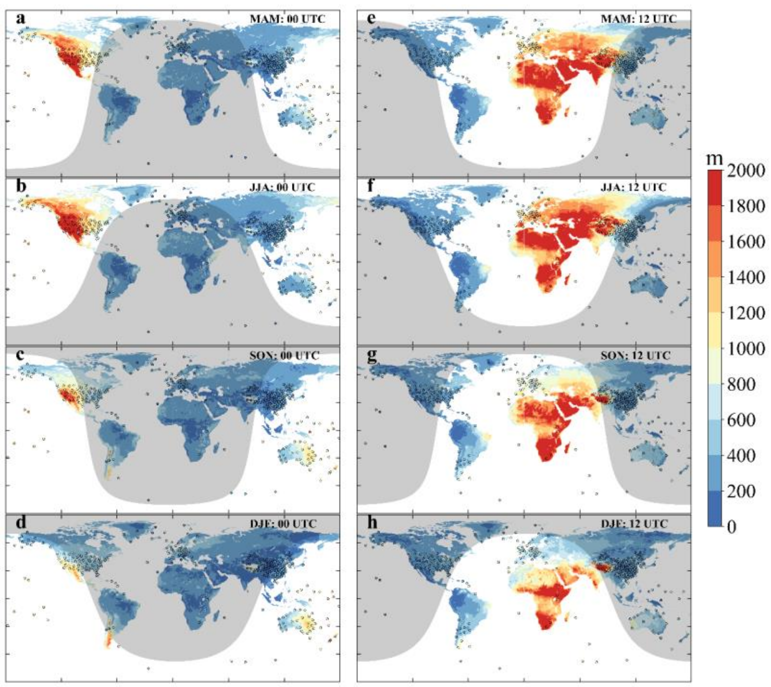

Figure 8. Spatial distribution of the PBLH at 0000 (a-d), and 1200 UTC (e-h) in four seasons over land ~~variations~~ produced by the merged algorithms proposed here ~~in four seasons of 0000 UTC (a-c), 0600 UTC (e-h), 1200 UTC~~ (i-l)~~, and 1800 UTC (m-p)~~.

带格式的: 两端对齐

设置了格式: 字体: 非加粗

The colored solid circles indicate the PBLH retrieved from high-resolution radiosondes. The shadow zones show nighttime regions, depending on the solar zenith angle on 15 April 2019 (MAM), 15 July 2019 (JJA), 15 October 2019 (SON), and 15 January 2019 (DJF). MAM, March–April–May; JJA, June–July–August; SON, September–October–November; DJF, December–January–February.

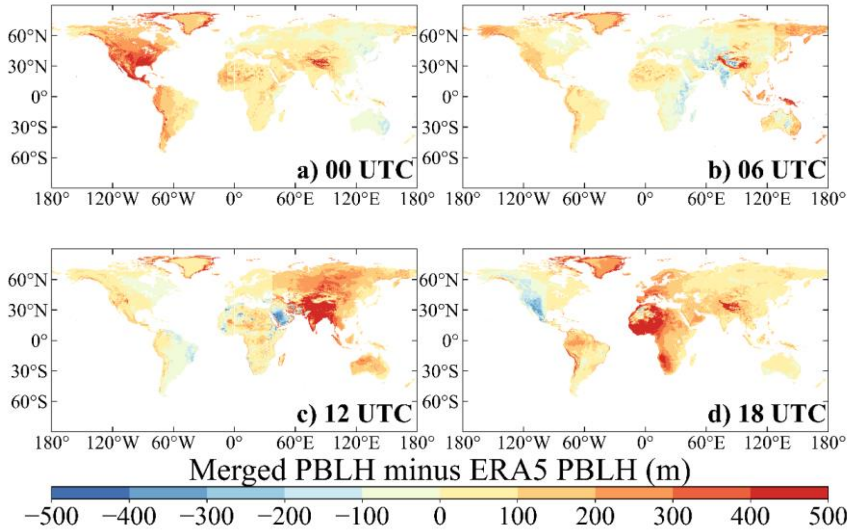

Figure 9. The spatial distributions of PBLH differences between the merged dataset and ERA5 reanalysis from the years 2011 to 2021 at 0000 ~~UTC~~ (a), 0600 ~~UTC~~ (b), 1200 ~~UTC~~ (c), and 1800 UTC (d).